Extraordinary Photoresponse in Two-Dimensional In_2Se_3 Nanosheets

Robin B. Jacobs-Gedrim, Mariyappan Shanmugam, Nikhil Jain, Christopher A. Durcan, Michael T. Murphy, Thomas M. Murray, Richard J. Matyi, Richard L. Moore, II, and Bin Yu*

SUNY College of Nanoscale Science and Engineering, State University of New York, Albany, New York 12203, United States

ABSTRACT We demonstrate extraordinary photoconductive behavior in two-dimensional (2D) crystalline indium selenide (In_2Se_3) nanosheets. Photocurrent measurements reveal that semiconducting In_2Se_3 nanosheets have an extremely high response to visible light, exhibiting a photoresponsivity of 3.95×10^2 A·W^{-1} at 300 nm with an external quantum efficiency greater than 1.63×10^5 % at 5 V bias. The key figures-of-merit exceed that of graphene and other 2D material-based photodetectors reported to date. In addition, the photodetector has a fast response time of 1.8×10^{-2} s and a specific detectivity of 2.26×10^{12} Jones. The photoconductive response of α-In_2Se_3 nanosheets extends into ultraviolet, visible, and near-infrared spectral regions. The high photocurrent response is attributed to the direct band gap (E_G = 1.3 eV) of In_2Se_3 combined with a large surface-area-to-volume ratio and a self-terminated/native-oxide-free surface, which help to reduce carrier recombination while keeping fast response, allowing for real-time detection under very low-light conditions.

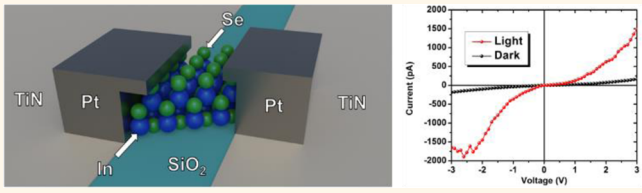

KEYWORDS: indium selenide · two-dimensional semiconductors · photodetectors · nanosheets · responsivity

Since the discovery of graphene, a number of two-dimensional (2D) crystals with distinct properties have been explored as potential material candidates for nanoscale electronics and optoelectronics.[1−3] An extensive set of layer-structured crystals exist, ranging from group IV elements to binary/ternary/quaternary compounds.[4] Transition-metal dichalcogenides (TMDCs) and transition-metal trichlcogenides (TMTCs) encompass the largest group of layered crystals.[5] TMDCs/TMTCs consist of a transition-metal atom (*e.g.*, Mo, W, Ga, Ti, Nb, Bi, and In) coordinated with a chalcogen atom (*e.g.*, S, Se, and Te). With more than 40 available compounds, these crystals exhibit strong covalent bonds for an in-plane lattice and weak *van der Waals* interactions between the neighboring layers. The unique layered structures offer the possibility to readily extract atomically thin monolayers of few-layer nanosheets from the parent bulk material *via* chemical[6] or micromechanical exfoliation methods.[7] Nanosheets of 2D semiconductor TMDCs show intriguing material behaviors, which are strongly dependent on the number of layers (or thickness). For example, MoS_2 changes from indirect band gap ($E_G \approx 1.3$ eV) in few-layer nanosheets to direct band gap ($E_G \approx 1.82$ eV) in monolayer nanosheets.[8] Distinctive physical properties of MoS_2 monolayer nanosheets have been reported.[9−12] GaS nanosheets show enhanced carrier mobility with decreasing thickness due to reduction in effective mass at the valence band maximum, which is favorable for designing highly responsive photodetectors.[13] Contrary to traditional bulk or thin-film semiconductors, layered crystals are expected to have the following advantages: (i) *Scalability*. 2D systems allow for self-limiting assembly with atomic-level thickness control, making ultimate material scaling possible. (ii) *Perfect interface*. Due to the self-terminated atomic bonds at the surface of 2D crystal systems, the amount of surface states is negligible and native oxide formation is generally forbidden. This is attractive for low-scattering/low-recombination systems. (iii) *Low defectivity*. 2D nanosheets exhibit a high degree of crystallinity. Certain types of commonly observed line/planar crystallographic defects in bulk or thin-film material systems are often absent in 2D nanoscale crystals. These unique attributes make 2D semiconductor nanosheets a new class of emerging materials with superior quality, key to electronic, optoelectronic, and photovoltaic applications. Recently, optoelectronic devices were reported using various types of 2D layered semiconductors

* Address correspondence to byu@albany.edu.

Received for review September 26, 2013 and accepted December 21, 2013.

Published online December 21, 2013
10.1021/nn405037s

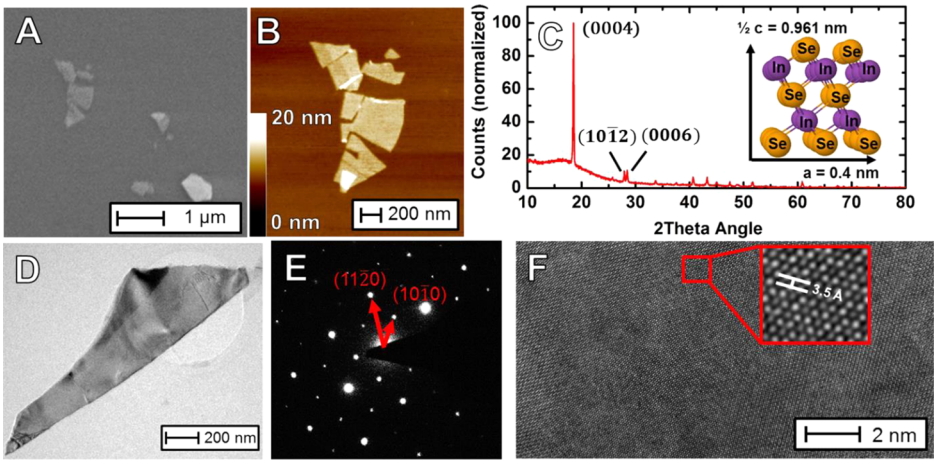

Figure 1. (A) Scanning electron micrograph of atomically thin In_2Se_3 nanosheets. (B) Corresponding AFM image with flake thickness measured to be ~3.9 nm, or four quintuple layers. (C) Measured XRD spectrum of In_2Se_3 source material indicating the bulk material is primarily α-phase (hexagonal symmetry $a = 4.05$ Å $c = 1.923$ Å). The inset of (C) shows the atomic bonding of the quintuple layers of α-In_2Se_3, which consists of 1/2 a traditional unit cell along the *c* axis and two unit cells along each of the *a* and *b* directions. (D) TEM image of an In_2Se_3 nanosheet over a holey carbon grid. (E) SAED pattern of the nanosheet suggests high crystallinity with the beam roughly parallel to the *c* axis of the crystal. The atomic spacing along the [10$\bar{1}$0] direction was measured to be 0.35 nm and that along the [11$\bar{2}$0] direction to be 0.19 nm. (F) HR-TEM image of the nanosheet showing excellent crystallinity with no apparent lattice defects. The inset is a zoomed-in portion of the region in which the lattice parameter was measured in the [1$\bar{1}$00] direction.

(*e.g.*, GaS,[13] GaSe,[14] MoS_2,[15] In_2Te_3,[16] and $TiSe_2$[17]), prepared by mechanical/chemical exfoliation or chemical vapor deposition (CVD), showing largely improved performance.

Indium(III) selenide (In_2Se_3) is a binary sesquichalcogenide III−VI compound semiconductor that has been extensively exploited in multiple applications including solar energy harvesting,[18,19] nonvolatile phase-change memory,[20] and optoelectronics.[21] In particular, In_2Se_3 is a desirable materials for photodetection due to the optimum direct-band gap ($E_G = 1.3$ eV), efficient absorption, and sensitivity.[22] In bulk or thin-film In_2Se_3 these properties largely depend on phase and stoichiometry,[23,24] leading to inconsistent results. There are five known crystalline forms ($\alpha, \beta, \gamma, \delta, \kappa$)[25] of In_2Se_3. The two common forms are α-phase and β-phase, which share a layered crystallographic structure, differing in lattice parameters and material properties.

While the production of 2D In_2Se_3 nanosheets *via* micromechanical exfoliation has been reported in recent literature,[26] the optical and electrical properties of this novel 2D layered semiconductor are largely unknown. In general, low-dimensional nanostructures yield high responsivity to light due to large surface-to-volume ratio and quantum confinement effects. Single-crystalline In_2Se_3 nanowires have been reported to exhibit consistently better light-response behavior than their bulk (or thin-film) counterparts.[27,28] The wide-spectrum response of In_2Se_3 nanowires suggests quantum confinement plays a key role in the photocurrent response of the devices. The high performance demonstrated in nanowire photodetectors is promising, but the one-dimensional configuration poses major limitations in manufacturability. Other than the issues with deterministic placement, it has been observed that In_2Se_3 nanowires may grow in-plane or perpendicular-to-plane, resulting in metallic or semiconducting behavior accordingly.[29] In addition, dangling bonds at the nanowire surface are prone to oxidation under ambient condition, which broadens optical response, but also limits response time and responsivity.[30] In this article, two-dimensional semiconducting In_2Se_3 nanosheets are exploited as the material for photodetection. Micromechanical exfoliation, similar to that used to obtain graphene, is employed to produce α-In_2Se_3 nanosheets. The demonstrated few-layer In_2Se_3 photodetector exhibits ultrahigh responsivity, which is significantly better than that of the recently reported photodetectors made on graphene[31] or other 2D layered semiconductors.[13,14,31−34]

RESULTS

Few-to-monolayer In_2Se_3 nanosheets were obtained through exfoliation of commercial-grade In_2Se_3. Nanosheets were identified using scanning electron microscopy (SEM) with thickness measured using atomic force microscopy (AFM). The collected data from X-ray diffractometry (XRD) and selected-area electron diffraction (SAED), combined with high-resolution images acquired from transmission electron microscopy (TEM), were used to examine the crystallographic phase and morphology information of the quintuple layers. Figure 1A is the SEM image of the exfoliated few-layer In_2Se_3 nanosheets on SiO_2/Si. The micrograph was taken at a low accelerating voltage (1 kV) so that ultrathin sheets could be identified by secondary electron absorption contrast. Figure 1B is an AFM map showing the locally measured thickness

(~3.9 nm; see Supporting Information) on the same sample identified in the SEM image in Figure 1A.

Material characterization was conducted to determine the crystallographic phase of the as-prepared In_2Se_3 nanosheets. It is known that multiple phases of stoichiometric In_2Se_3 exist (α, β, γ, κ, and δ) with varying lattice parameters: α-phase: a = 4.02 Å, c = 19.23 Å;[35] β-phase: a = 4.01 Å, c = 19.22 Å;[36] γ-phase: a = 7.12 Å, c = 19.38 Å;[37] κ-phase: a = 8.09 Å, c = 19.85 Å;[25] and δ-phase: a = 4.00 Å, c = 19.28 Å.[38] While discrepancies do exist in the literature, it is necessary to carefully determine the crystallographic phase of the In_2Se_3 nanosheets. Figure 1C shows the XRD data from the In_2Se_3 source material crushed into powder form (on glass substrate). The observed peaks exhibit primarily the characteristic of α-In_2Se_3, yet also that of other crystallographic phases, which is expected for powder and bulk In_2Se_3 in which the existence of pure phase is thermodynamically unfavorable. The inset of Figure 1C shows schematically the atomic model of the quintuple-layer lattice in α-In_2Se_3 with a total thickness of ~0.925 nm along the c axis, indicating that the thickness of nanosheets (3.9 nm) corresponds to that of four quintuple layers. Figure 1D shows the TEM image of a single nanosheet used to generate the SAED pattern, depicted in Figure 1E. The following key information can be drawn from the data: The [0001] axis of the flake is nearly parallel to the beam path (as indicated by the 60-degree angles between these adjacent diffraction spots), and the lengths of $[10\bar{1}0]$ and $[11\bar{2}0]$ axes were 0.35 and 0.19 nm, respectively, which match the parameters of α-phase In_2Se_3. This gives a clear indication that the nanosheet is not of mixed phase and in fact is highly crystalline (if not single crystalline). Further, the SAED patterns confirm that there is only one crystallographic orientation represented in the nanosheet, regardless of the number of quintuple layers. Figure 1F shows the HR-TEM image in which no apparent defects are visible and the atomic spacing (0.35 nm) matches the lattice characteristic of α-In_2Se_3 in the $[1\bar{1}00]$ direction.

The stoichiometry and chemical composition of the In_2Se_3 nanosheets were further characterized by energy-dispersive X-ray spectrometry (EDS) and Auger electron spectrometry (AES). Figure 2A shows the same nanosheet (at higher magnification) as in Figure 1D, focusing on the area suspended over a hole in the carbon film. The inset shows the elemental mapping results of the nanosheet, generated by EDS. The results indicate both indium and selenium are homogeneously distributed throughout the sample. Figure 2B is the AES spectrum of the In_2Se_3 nanosheet. While Auger electrons are generated at the surface of a sample and are highly sensitive to chemical composition in that region, for layered α-phase In_2Se_3 this means Auger electrons are generated within the top 2−5 quintuple layers and from surface contamination,

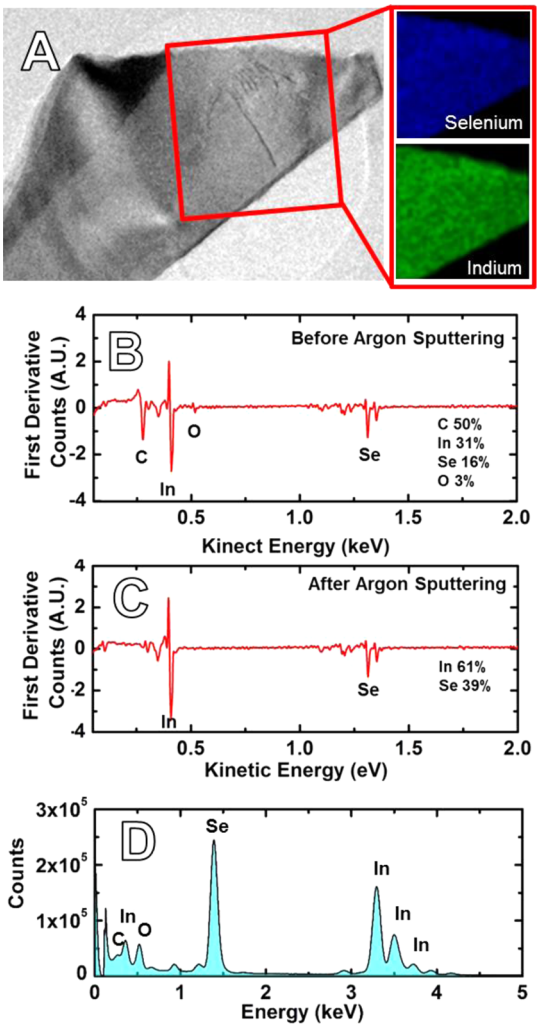

Figure 2. (A) TEM image of the In_2Se_3 nanosheet as shown in Figure 1D. The inset is the elemental mapping result generated from energy-dispersive X-ray spectroscopy, demonstrating homogeneous selenium and indium contents. (B) Auger spectra of a single sheet of In_2Se_3 showing a less than monolayer amount of carbon and oxygen contamination at the surface. (C) Auger spectra of the nanosheet after moderate argon sputtering to remove carbon. (D) EDS spectra of the whole In_2Se_3 nanosheet. The result indicates nearly stoichiometric In_2Se_3, supporting the Auger measurement.

if present. The measured AES data of the nanosheet display the dominant peaks for indium and selenium (with minor peaks for carbon and oxygen). The oxygen peak is too small to represent the presence of a native oxide, which would be otherwise indicated by a dominant peak, typically higher than other peaks. We attribute the suppression of oxide formation to the surface with self-terminated atomic bonds (*i.e.*, saturated or free of dangling bonds) of the layer-structured In_2Se_3 nanosheet. In contrast, In_2Se_3 nanowires, due to unsaturated bonds on the surface, almost always form an oxide shell under ambient exposure, or even during the growth process. The cleaved surfaces of an α-In_2Se_3 nanosheet are exceptionally insensitive to the environment, taking two to three years to form a native

oxide in ambient condition.[37] Argon-based ion milling was used to remove any adventitious surface contamination on the nanosheet after the initial AES measurement. The ion gun was operated at 2.5 kV and ~1.1 μA, rastered over a 2 × 2 mm area, resulting in a sputter rate of ~60 Å/min for SiO_2 (much less for In_2Se_3). After argon sputtering, the sample showed only In and Se peaks in the stoichiometric In_2Se_3 ratio, as shown in Figure 2C. This indicates that carbon and oxygen contaminants on the nanosheet surface were completely removed. The discrepancy in the In-to-Se ratio before [Figure 2B] and after the surface etching process [Figure 2C] can be explained by attenuation of the low-energy indium Auger electrons with carbon contaminant. The removal of contaminant results in a nanosheet surface close to stoichiometric In_2Se_3 yet with a small amount of selenium deficiency. Figure 2D is the measured EDS spectrum of the nanosheet, which indicates only a small amount of carbon and oxygen contamination (including some signal from the TEM grid) and relatively pure indium and selenium, qualitatively supporting the Auger measurement.

To explore the photoconductive behavior of In_2Se_3 nanosheets, we fabricated photodetectors on the SiO_2/Si substrate. Interdigitated electrodes were fabricated on a 100 nm SiO_2/p-type silicon substrate using the damascene process in which TiN was deposited to completely fill in the oxide trenches and polished to yield an ultraflat receiving structure for the transferred nanosheets. An electron beam was used to decompose platinum using a gas-phase metal–organic precursor to extend ultrathin local contacts to the nanosheet from the interdigitated electrodes. A schematic of the photodetector can be viewed in Figure 3A. The top-view SEM image of the device is shown in Figure 3B (from which critical in-plane dimensions were extracted). The device length is measured to be ~240 nm, and the total active area is 0.108 μm^2 (see Supporting Information). Figure 3C shows the two-dimensional AFM mapping result. The solid white line indicates the location for line scan by which the thickness of the nanosheet was measured from the step height (as shown in Figure 3D). Due to the contact height in the AFM image in Figure 3C, the integral gain on the AFM had to be set at ~1.0, resulting in artifacts at the nanosheet edges in the line scan in Figure 3D. The height of the nanosheet was measured from the right side of the scan (the AFM tip travels from right to left) to the center of the nanosheet. The measured nanosheet is ~10 nm thick, corresponding to 10 quintuple layers (or equivalently 5 conventional unit cells).

Figure 4A are the I–V characteristics of the In_2Se_3 nanosheet photodetector measured under dark and illuminated conditions. Both the dark and illuminated I–V curves pass through the origin, precluding the possibility that a photovoltaic effect contributes to the observed photoconduction (zero short-circuit current).

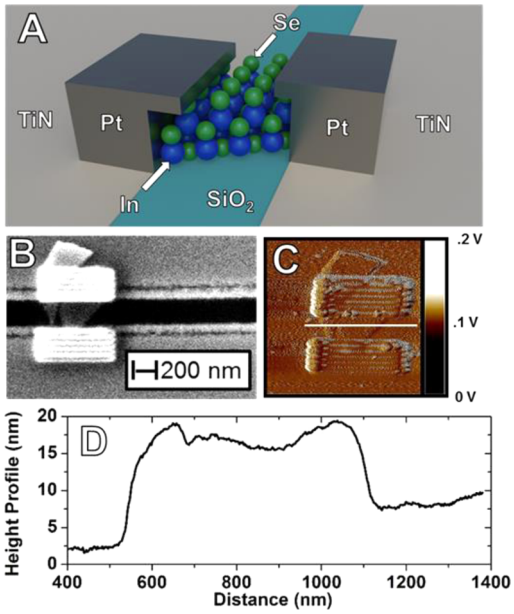

Figure 3. (A) Schematic of the α-In_2Se_3 nanosheet photodetector. (B) SEM of the photodetector from which the 0.041 μm^2 active area and 240 nm device length were determined. (C) AFM mapping image of the photodetector with the white line indicating the location of the line scan. (D) Measured step height profile from the AFM line scan as indicated in (C) showing that the nanosheet is approximately 10 quintuple layers thick.

This could be attributed to the high level of amorphous carbon content, up to 60%, in the deposited Pt, which lowers the metal work function similar to the Fermi level of In_2Se_3, measured ~4.35 eV in the bulk.[38] Under white light illumination (source: EKE 150 W), the photodetector current increases drastically, particularly at high voltage bias, shown as the red line in Figure 4A.

To measure the photodetector response time, a green LED controlled by a pulse generator was used to direct light onto the nanosheet device. Figure 4B shows the transient current waveform in response to a series of cycles with alternating ON and OFF of the LED light source. The In_2Se_3 nanosheet photodetector exhibits a repeatable and reasonably stable response to incident light. Figure 4C shows the single-cycle response of light ON and OFF. The response time was calculated by averaging the duration values between light-ON and light-OFF (taking 10% to 90% photocurrent change for the rise times and 90% to 10% for the fall times). The measured rise and fall times were 18 and 73 ms, respectively, demonstrating excellent response performance for a resistor-mode photodetector.

To further benchmark the photodetector performance, two other key figures of merit (FOMs) were measured: responsivity (R_λ) and specific detectivity (D^*). When used in photoconductive mode, the responsivity is the ratio of generated photocurrent to incident light power. The wavelength dependence can also be presented by the EQE, or the ratio of the number of photogenerated carriers to the number of

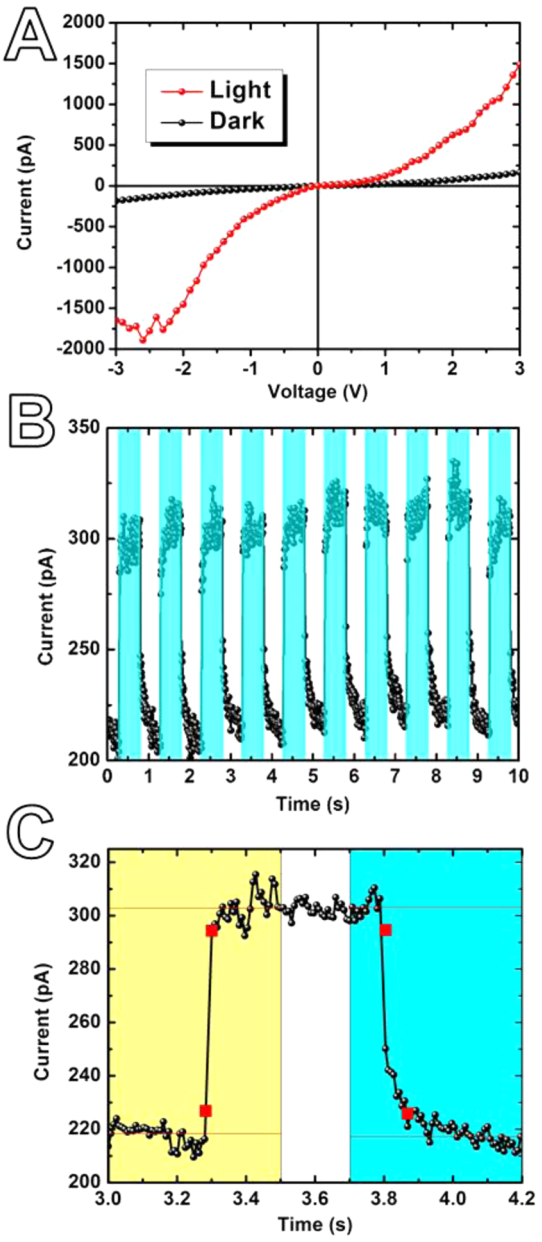

Figure 4. (A) Photocurrent response of the detector to a broad-spectrum light source (with reference to the dark current). (B) Transient current waveform under a series of light pulses generated from the green LED showing fast and repeatable photocurrent response. The blue-colored regions indicate the time interval during which the LED was in the ON state. (C) Single-cycle response characteristics of the photodetector for rise/fall time analysis.

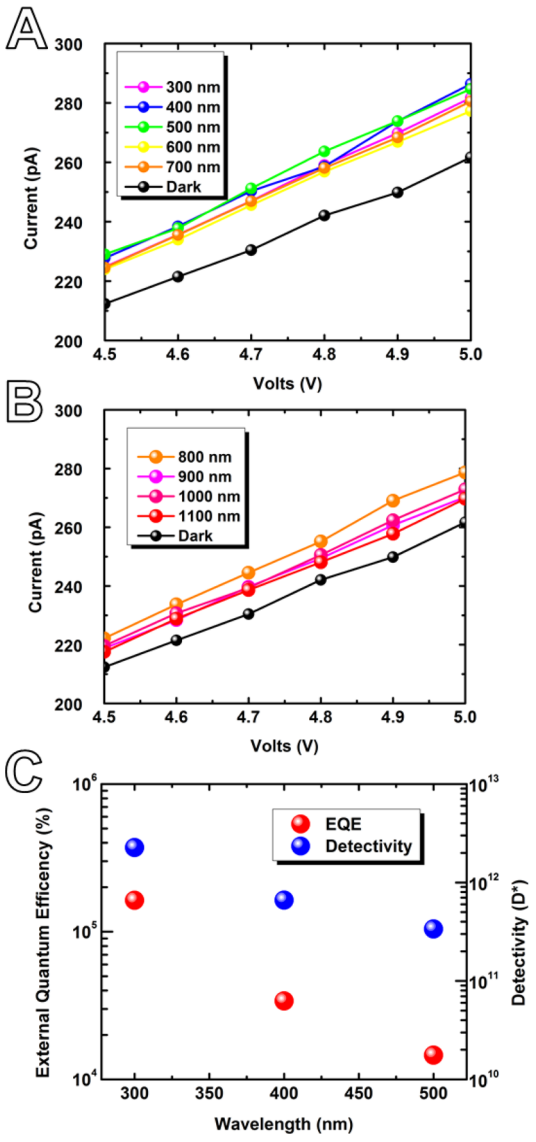

Figure 5. (A) Photocurrent response of the photodetector to monochromatic light in both the visible and ultraviolet spectral range. (B) Photocurrent response to monochromatic light in the near-infrared spectral range.The voltage sweep in both (A) and (B) ranges from −5 V to +5 V; the full *I*−*V* sweep is included in the Supporting Information. (C) Key device figures-of-merit, EQE and specific detectivity, measured at different wavelengths under monochromatic illumination.

incident photons. Figure 5A is the photocurrent response as a function of biasing voltage (applied across the nanosheet) at different wavelengths in the UV−visible range, whereas Figure 5B shows the response of similar pattern in the near-infrared (NIR) range. The demonstrated photoconductive response appears to be high across the broad spectra. In our experiment, the irradiance of the monochrome light source was calibrated with a ThorLabs DET25K GaP detector within the spectral range of 100−550 nm. The measured light power density of the monochrome light was found to be 0.469 $W \cdot m^{-2}$ at 300 nm, 2.08 $W \cdot m^{-2}$ at 400 nm, and 3.61 $W \cdot m^{-2}$ at 500 nm, which are expected values of the light source and the monochromator from specifications. The responsivity and EQE were extracted from the photocurrent data (shown in Figure 5A) using the relation $R_\lambda = I_\lambda/P_\lambda A$ where I_λ is the photocurrent, P_λ is the light power density, and A is the surface area of the photodetector.[27] The responsivity at 5 V was measured to be 3.95×10^3 $A \cdot W^{-1}$ at 300 nm, 1.1×10^2 $A \cdot W^{-1}$ at 400 nm, and 5.9×10^1 at 500 nm wavelength, respectively. The corresponding EQE was calculated from the responsivity with EQE = $hcR_\lambda/(e\lambda)$ where h is Planck's constant, c is the

TABLE 1. Comparison of Key Device Performance Figures-of-Merit and Band Gap of the Recently Reported 2D Material-Based Photodetectors

2D layered material	measurement condition	responsivity(A/W)	EQE (%)	specific detectivity (*D**)	response time (s)	band gap (eV)	source
graphene	532 nm,0.1 V	8.61					31
GaSe	254 nm,5 V	2.8	1367		0.02	2.11 (indirect)	14
GaS	254 nm,2 V	4.2	2050	1×10^{13}	0.003	3.05 (indirect)	13
MoS_2	N/A,1 V	0.000 42			0.050	1.8 (direct)	33
In_2Se_3	300 nm,5 V	395	163 000	2.26×10^{12}	0.018	1.3 (direct)	this work

speed of light, e is the electron charge, and λ is the wavelength.[27] The EQE of the In_2Se_3 nanosheet photodetector (at 5 V) was calculated to be 1.63×10^5 % at 300 nm, 3.4×10^4 % at 400 nm, and 1.46×10^4 % at 500 nm, respectively. The specific detectivity (D^*) is the characteristic detectivity (D) multiplied by the square root of the photodetector area (A) ($D^* = D\sqrt{A}$). Here D is the inverse of noise-equivalent power (NEP). The NEP, defined as the minimum input optical power to generate photocurrent equal to the RMS noise current in 1 Hz bandwidth, is essentially the minimum detectable signal. The specific detectivity allows different systems to be compared independent of device area and band width. The specific detectivity (D^*) in the unit of Jones was calculated using $D^* = R_\lambda A^{1/2}/(2eI_d)^{1/2}$, where R_λ is the responsivity, A is the device effective area, and I_d is the dark current.[13] The specific detectivity (at 5 V) was calculated to be $\sim 2.26 \times 10^{12}$ Jones at 300 nm, 6.26×10^{11} Jones at 400 nm, and 3.37×10^{11} Jones at 500 nm wavelength, respectively. Figure 5C shows the EQE and specific detectivity at each wavelength under monochromatic illumination.

DISCUSSION

Table 1 is the comparison of key device FOMs among recently reported 2D material-based photodetectors. The α-In_2Se_3 nanosheets demonstrated in this work exhibit significantly higher spectral responsivity and external quantum efficiency as compared with other 2D photoresistor systems[13,14,31−34] and faster response than monolayer MoS_2. We attribute the exceptionally high photoresponse in the In_2Se_3 nanosheet to the material's 1.3 eV direct band gap, the smallest among all the reported 2D layered semiconductors, which promotes efficient generation of photocarriers across a broad range of photon energies.[34] 2D In_2Se_3 nanosheets demonstrated in this work show significantly higher responsivity than undoped In_2Se_3 1D nanowires and thin films, however.[28,39,40] We attribute this result to increased surface-area-to-volume ratio ($\sim 2.13 \times 10^8$ m^{-1}), much greater than bulk/thin film and nanowires, and *self-terminated, native-oxide-free surfaces*, which help to reduce the probability of carrier recombination. While the longer carrier lifetime has a positive effect on responsivity, the response time of the detector is increased in comparison to In_2Se_3 nanowires with a native oxide at the surface.[27] The small channel length (~240 nm) also facilitates carrier transport and fast response. While we have limited our discussion to photodetectors operating in a photoresistor functional mode, field effect can be used to increase the photocurrent gain of the In_2Se_3 nanosheets, similar to what has been observed in Si, ZnO nanowires and MoS_2 monolayers (see Supporting Information).[34,41,42]

CONCLUSION

An exceptional photocurrent response in 2D semiconducting α-In_2Se_3 nanosheets has been demonstrated. Ultrathin (few quintuple layers), highly crystalline In_2Se_3 nanosheets were prepared by micromechanical exfoliation. Key device figures-of-merit were benchmarked and compared with all other 2D material-based photodetectors reported recently. To our best knowledge, the spectral responsivity and EQE of α-In_2Se_3 nanosheet well exceed that of graphene and other layered semiconductors including MoS_2, GaS, and GaSe, while exhibiting comparable response characteristics. The results indicate that semiconducting In_2Se_3 nanosheets with single-crystallographic phase, ultrahigh crystallinity, and native-oxide-free surfaces can be prepared for prototyping high-performance photodetectors. Compared with nanowires, the resistance to oxidation on cleaved surfaces in a 2D nanosheet is a crucial advantage, making devices less susceptible to contamination or parameter drifting in ambient condition. The α-In_2Se_3 nanosheet-based photodetectors represent a promising direction toward broad-spectrum real-time imaging under low-light conditions. In addition, the material may find other potential applications including UV−vis−NIR spectroscopy, biomedical imaging, high-resolution video recording, aerial photography, astronomy, and photovoltaics.

EXPERIMENTAL METHODS

In_2Se_3 particles with 4−6 mm diameter (Alfa Aesar, 99.999% purity) were used as the source material. The outer layer of the In_2Se_3 particles appeared dull gray in color due to a native oxide formed on the surface. A razor blade was used to cleave away the outer surface, revealing one that appeared to be dark gray in color with a metallic sheen. In_2Se_3 nanosheets were then prepared from the cleaved sample by using micromechanical exfoliation (the Scotch tape method) onto the p-type doped silicon substrate (covered with a 100 nm thermally grown silicon

dioxide layer). Titanium nitride (TiN) interdigitated electrodes were formed in the prefabricated SiO_2 trenches by a damascene process developed at the nanofab facility, Center for Semiconductor Research (CSR), College of Nanoscale Science and Engineering. The platinum (Pt) metal lines, serving as contact extensions, were directly written by a combinational SEM/FIB (FEI Dualbeam 600) using a 15 kV electron beam to decompose the precursor of methylcyclopentadienyl (trimethyl). Material characterization was performed using AFM (Bruker Dimension 3100), XRD (Bruker), STEM (FEI Titan G2 60-300), and an Auger spectrometer (Perkin-Elmer model 680). All photocurrent measurements were performed at room temperature in air using a 150 W broad-spectrum light source (EKE), a green LED, a semiconductor analyzer (Agilent B1500), and a monochromator (Oriel instruments) calibrated with a GaP photodetector (Thor DET25K).

Conflict of Interest: The authors declare no competing financial interest.

Supporting Information Available: Additional optoelectronic characterization and experimental details are included. This material is available free of charge *via* the Internet at http://pubs.acs.org.

Acknowledgment. We acknowledgment Center for Semiconductor Research (CSR), College of Nanoscale Science & Engineering, for device fabrication. R.B.J.-G. thanks C. Settens for help with XRD measurements, A. Hmiel for 3D rendered images, and V. Tokronov for useful discussions.

REFERENCES AND NOTES

1. Geim, A. K.; Novoselov, K. S. The Rise of Graphene. *Nat. Mater.* **2007**, *6*, 183–191.
2. Xu, M.; Liang, T.; Shi, M.; Chen, H. Graphene-Like Two-Dimensional Materials. *Chem. Rev.* **2013**, *113*, 3766–3798.
3. Wang, Q. H.; Kalantar-Zadeh, K.; Kis, A.; Coleman, J. N.; Strano, M. S. Electronics and Optoelectronics of Two-Dimensional Transition Metal Dichalcogenides. *Nat. Nanotechnol.* **2012**, *7*, 699–712.
4. Koski, K. J.; Cui, Y. The New Skinny in Two-Dimensional Nanomaterials. *ACS Nano* **2013**, *7*, 3739–3743.
5. Radisavljevic, B.; Radenovic, A.; Brivio, J.; Giacometti, V.; Kis, A. Single-Layer MoS_2 Transistors. *Nat. Nanotechnol.* **2011**, *6*, 147–150.
6. Coleman, J. N.; Lotya, M.; O'Neill, A.; Bergin, S. D.; King, P. J.; Khan, U.; Young, K.; Gaucher, A.; De, S.; Smith, R. J.; *et al.* Two-Dimensional Nanosheets Produced by Liquid Exfoliation of Layered Materials. *Science* **2011**, *331*, 568–571.
7. Yoon, Y.; Ganapathi, K.; Salahuddin, S. How Good Can Monolayer MoS_2 Transistors Be? *Nano Lett.* **2011**, *11*, 3768–3773.
8. Das, S.; Chen, H.-Y.; Penumatcha, A. V.; Appenzeller, J. High Performance Multilayer MoS_2 Transistors with Scandium Contacts. *Nano Lett.* **2013**, *13*, 100–105.
9. Splendiani, A.; Sun, L.; Zhang, Y.; Li, T.; Kim, J.; Chim, C. Y.; Galli, G.; Wang, F. Emerging Photoluminescence in Monolayer MoS_2. *Nano Lett.* **2010**, *10*, 1271.
10. Brivio, J.; Alexander, D. T. L.; Kis, A. Ripples and Layers in Ultrathin MoS_2 Membranes. *Nano Lett.* **2011**, *11*, 5148–5153.
11. Najmaei, S.; Liu, Z.; Ajayan, P. M.; Lou, J. Thermal Effects on the Characteristic Raman Spectrum of Molybdenum Disulfide (MoS_2) of Varying Thicknesses. *Appl. Phys. Lett.* **2012**, *100*, 013106.
12. Hwang, H.; Kim, H.; Cho, J. MoS_2 Nanoplates Consisting of Disordered Graphene-like Layers for High Rate Lithium Battery Anode Materials. *Nano Lett.* **2011**, *11*, 4826–4830.
13. Hu, P.; Wang, L.; Yoon, M.; Zhang, J.; Feng, W.; Wang, X.; Wen, Z.; Idrobo, J. C.; Miyamoto, Y.; Geohegan, D. B. Highly Responsive Ultrathin GaS Nanosheet Photodetectors on Rigid and Flexible Substrates. *Nano Lett.* **2013**, *13*, 1649–1654.
14. Hu, P.; Wen, Z.; Wang, L.; Tan, P.; Xiao, K. Synthesis of Few-Layer GaSe Nanosheets for High Performance Photodetectors. *ACS Nano* **2012**, *6*, 5988–5994.
15. Lee, H. S.; Min, S.-W.; Chang, Y.-G.; Park, M. K.; Nam, T.; Kim, H.; Kim, J. H.; Ryu, S.; Im, S. MoS_2 Nanosheet Phototransistors with Thickness-Modulated Optical Energy Gap. *Nano Lett.* **2012**, *12*, 3695–3700.
16. Wang, Z.; Safdar, M.; Jiang, C.; He, J. High-Performance UV-Visible-NIR Broad Spectral Photodetectors Based on One-Dimensional In_2Te_3 Nanostructures. *Nano Lett.* **2012**, *12*, 4715–4721.
17. Goli, P.; Khan, J.; Wickramaratne, D.; Lake, R. K.; Balandin, A. A. Charge Density Waves in Exfoliated Films of van der Waals Materials: Evolution of Raman Spectrum in $TiSe_2$. *Nano Lett.* **2012**, *12*, 5941–5945.
18. Segura, A.; Guesdon, J. P.; Besson, J. M.; Chevy, A. Photovoltaic Effect in InSe Application to Solar Energy Conversion. *Rev. Phys. Appl.* **1979**, *14*, 253–257.
19. Lakshmikumar, S. T.; Rastogi, A. C. Selenization of Cu and In Thin Films for the Preparation of Selenide Photo-Absorber Layers in Solar Cells Using Se Vapour Source. *Sol. Energy Mater. Sol. Cells* **1994**, *32*, 7–19.
20. Yu, B.; Ju, S.; Sun, X.; Ng, G.; Nguyen, T. D.; Meyyappan, M.; Janes, D. B. Indium Selenide Nanowire Phase-Change Memory. *Appl. Phys. Lett.* **2007**, *91*, 133119.
21. Wang, J.-J.; Cao, F.-F.; Jiang, L.; Guo, Y.-G.; Hu, W.-P.; Wan, L.-J. High Performance Photodetectors of Individual InSe Single Crystalline Nanowire. *J. Am. Chem. Soc.* **2009**, *131*, 15602–15603.
22. Sánchez-Royo, J. F.; Segura, A.; Lang, O.; Schaar, E.; Pettenkofer, C.; Jaegermann, W.; Roa, L.; Chevy, A. Optical and Photovoltaic Properties of Indium Selenide Thin Films Prepared by van der Waals Epitaxy. *J. Appl. Phys.* **2001**, *90*, 2818–2823.
23. Sreekumar, R.; Jayakrishnan, R.; SudhaKartha, C.; Vijayakumar, K. P.; Khan, S. A.; Avasthi, D. K. Enhancement of Band Gap and Photoconductivity in Gamma Indium Selenide Due to Swift Heavy Ion Irradiation. *J. Appl. Phys.* **2008**, *103*, 023709.
24. de Groot, C. H.; Moodera, J. S. Growth and Characterization of a Novel In_2Se_3 Structure. *J. Appl. Phys.* **2001**, *89*, 4336–4340.
25. Jasinski, J.; Swider, W.; Washburn, J.; Liliental-Weber, Z.; Chaiken, A.; Nauka, K.; Gibson, G. A.; Yang, C. C. Crystal Structure of k-In_2Se_3. *Appl. Phys. Lett.* **2002**, *81*, 4356–4358.
26. Tao, X.; Gu, Y. Crystalline-Crystalline Phase Transformation in Two-Dimensional In_2Se_3 Thin Layers. *Nano Lett.* **2013**, 10.1021/nl400888p.
27. Zhai, T.; Fang, X.; Liao, M.; Xu, X.; Li, L.; Liu, B.; Koide, Y.; Ma, Y.; Yao, J.; Bando, Y.; *et al.* Fabrication of High-Quality In_2Se_3 Nanowire Arrays toward High-Performance Visible-Light Photodetectors. *ACS Nano* **2010**, *4*, 1596–1602.
28. Li, Q. L.; Li, Y.; Gao, J.; Wang, S. D.; Sun, X. H. High Performance Single In_2Se_3 Nanowire Photodetector. *Appl. Phys. Lett.* **2011**, *99*, 243105.
29. Peng, H.; Xie, C.; Schoen, D. T.; Cui, Y. Large Anisotropy of Electrical Properties in Layer-Structured In_2Se_3 Nanowires. *Nano Lett.* **2008**, *8*, 1511–1516.
30. Ho, C.-H.; Lin, C.-H.; Wang, Y.-P.; Chen, Y.-C.; Chen, S.-H.; Huang, Y.-S. Surface Oxide Effect on Optical Sensing and Photoelectric Conversion of α-In_2Se_3 Hexagonal Microplates. *ACS Appl. Mater. Interfaces* **2013**, *5*, 2269–2277.
31. Zhang, Y.; Liu, T.; Meng, B.; Li, X.; Liang, G.; Hu, X.; Wang, Q. J. Broadband High Photoresponse from Pure Monolayer Graphene Photodetector. *Nat. Commun.* **2013**, *4*, 1811.
32. Xia, F.;Mueller, T.;Lin, Y.;Valdes-Garcia, A. Ultrafast Graphene Photodetector. Avouris, P. *Nat. Nanotechnol.* **2009**, *4*, 839–843.
33. Yin, Z.; Li, H.; Li, H.; Jiang, L.; Shi, Y.; Sun, Y.; Lu, G.; Zhang, Q.; Chen, X.; Zhang, H. Single-Layer MoS_2 Phototransistors. *Nano* **2011**, *6*, 74–80.
34. Lopez-Sanchez, O.; Lembke, D.; Kayci, M.; Radenovic, A.; Kis, A. Ultra Sensitive Photo Detectors Based on Monolayer MoS_2. *Nat. Nanotechnol.* **2013**, 10.1038/nnano.2013.100.
35. Popović, S.; Tonejc, A.; Grzeta-Plenković, B.; Čelustka, B.; Trojko, R. Revised and New Crystal Data for Indium Selenides. *J. Appl. Crystallogr.* **1979**, *12*, 416–420.
36. Lutz, H.; Fischer, M.; Baldus, H.-P.; Blachnik, R. Zur Polymorphie des In_2Se_3. *J. Less-Common Met.* **1988**, *143*, 83–92.
37. Pfitzner, A.; Lutz, H. D. Redetermination of the Crystal Structure of Gamma-In_2Se_3 by Twin Crystal X-Ray Method. *J. Solid State Chem.* **1996**, *124*, 305–308.

38. Drapak, S. I.; Kovalyuk, Z. D. Asymmetric Current Flow in a Native Oxide/Indium Selenide Heterostructure. *Inorg. Mater.* **2011**, *47*, 1178–1182.
39. Sakalauskas, S.; Sodeika, A. Automated Measuring Instrument of the Surface Electric Potential and Potential Distribution. *Rev. Sci. Instrum.* **1998**, *69*, 466–468.
40. Zhai, T.; Ma, Y.; Li, L.; Fang, X.; Liao, M.; Koide, Y.; Yao, J.; Bando, Y.; Golberg, D. Morphology-Tunable In_2Se_3 Nanostructures with Enhanced Electrical and Photoelectrical Performances *via* Sulfur Doping. *J. Mater. Chem.* **2010**, *20*, 6630–6637.
41. Zhang, A.; Kim, H.; Cheng, J.; Lo, Y.-H. Ultrahigh Responsivity Visible and Infrared Detection Using Silicon Nanowire Phototransistors. *Nano Lett.* **2010**, *10*, 2117–2120.
42. Tsai, D.-S.; Lin, C.-A.; Lien, W.-C.; Chang, H.-C.; Wang, Y.-L.; He, J.-H. Ultrahigh Responsivity Broadband Detection Using Si Metal-Semiconductor-Metal Schottky Photodetectors Improved by ZnO Nanorod Arrays. *ACS Nano* **2011**, *5*, 7748–7753.